Northumbria Research Link

Northumbria
University
NEWCASTLE

Ultra-sensitive UV and H_2S dual functional sensors based on porous In_2O_3 nanoparticles operated at room temperature

Zhijie Li[1*], Shengnan Yan [1], Shouchao Zhang[1], Junqiang Wang [1], Wenzhong Shen[2], Zhiguo Wang[1], Yong Qing Fu[3*]

[1]School of Physics, University of Electronic Science and Technology of China, Chengdu 610054, PR China

[2]State Key Laboratory of Coal Conversion, Institute of Coal Chemistry, Chinese Academy of Science, Taiyuan, 030001, PR China

[3]Faculty of Engineering and Environment, Northumbria University, Newcastle Upon Tyne NE1 8ST, England, United Kingdom

Abstract

A dual functional sensor for detecting both UV light and H_2S gas was fabricated using the hexagonal phase porous In_2O_3 nanoparticles, which were prepared using the hydrothermal and calcination process. The porous In_2O_3 nanoparticles with large surface areas and pore volumes could provide plenty of active sites to produce much active oxygen species, which were beneficial for the UV light and H_2S gas sensing reactions, thus resulting in a good sensing performance. At room temperature, the dual functional sensor based on porous In_2O_3 nanoparticles exhibited ultra-high responses for sensing both UV light (with a wavelength of 365 nm) and H_2S gas. As a UV sensor, its response was 12886.0 for a UV power intensity of 1.287 mW/cm^2 and its detection limit was 0.013 mW/cm^2. As a H_2S gas sensor, the sensor exhibited an ultra-high response (26268.5 to 1 ppm H_2S) and a very low detection limit (1ppb of H_2S), and it also have excellent selectivity, reversibility and stability.

Keywords: In_2O_3, Nanoparticles, Porous, UV, H_2S, Sensor

1 Introduction

Ultraviolet (UV) light and toxic/poisonous gases are common environmental pollution sources, which are harmful threats to health of human beings [1,2]. Excessive exposure to UV light can cause a series of damages to human body functions, especially to body skin, eyes and immune system, and result in skin cancer. Toxic gases, such as hydrogen sulfide (H_2S), will cause disorder of normal physiological functions and damage of nerves and respiratory systems of human body, even at very low concentrations (for example, ppb levels). Therefore, it is critical to develop high performance sensors for real-time monitoring of both UV light and poisonous gases at room temperature with high sensitivity, excellent selectivity and low detection limit.

Sensors made of metal oxide nanostructures are normally effective to detect both UV light and poisonous gases, and developing new types of nanostructured sensing materials is one of the key factors for the successful application of these sensors. Many types of nanostructured metal oxides have been investigated to detect UV light or poisonous gases, and these include SnO_2 [3], ZnO [4,5], Fe_2O_3 [6], TiO_2 [7], NiO [8], In_2O_3 [9], CuO [10], and so on. Among these, In_2O_3 nanostructures have been proven to have good responses to UV light and various toxic gases. For example, Zhang et al. [9] reported that In_2O_3 nanoparticles based sensor exhibited a high response to UV light at room temperature. Yao et al. [11] made a H_2S gas sensor based on In_2O_3 nanoparticles, and the obtained detection limit was as low as 20 ppb at room temperature.

So far, various types of In_2O_3 nanostructures have been synthesized and used as

sensing materials, for example, nanofibers [12], nanowires [13], nanospheres [14], nanocubes [15,16], nanoplatelets [17] and nanoparticles [9,11, 18–20]. However, most reported In_2O_3 nanomaterials are relatively dense without porous nanostructures. Compared with the relatively dense metal oxides, the porous nanostructures have larger surface areas and more active adsorption sites [17]. These are beneficial to the production of surface-adsorbed oxygen species (such as O_2^-, O^- and O^{2-}), which are often the key factor to enhance the gas sensing properties of metal oxides based sensors. For an example, it was reported that porous α-Fe_2O_3 nanoparticles showed a better sensing performance than the dense α-Fe_2O_3 ones [21,22]. Due to this reason, much effort has been made so far to prepare and characterize porous In_2O_3 nanostructures for sensing applications [23–26]. For examples, Sun et al. [23] prepared mesoporous In_2O_3 using a nanocasting method, and obtained a significantly improved response to ethanol (with a detection limit of 0.05 at 220 ^oC) in comparison with the data from the bulk In_2O_3. Shanmugasundaram et al. [15] reported that mesoporous In_2O_3 nanocubes prepared using a hydrothermal method showed a superior sensitivity to H_2 at a very low concentration of 100 ppb. Recently Wang et al. [24] reported that the sensor made of In_2O_3 nanosheets with mesopores showed a high response of 213 toward 10 ppm NO_x with a low detection limit of 10 ppb at 120 ^oC. Zhang et al. [25] prepared hierarchical Au-loaded In_2O_3 porous nanocubes using a hydrothermal process, and the sensor made using these porous nanocubes showed a response of 37 to 100 ppm formaldehyde at 240 ^oC. Hyodo et al. [26] reported that sensors made of porous In_2O_3 powders prepared using ultrasonic-spray pyrolysis exhibited a better response to 10 ppm NO_2 than the

sensor made of the conventional In_2O_3 powders. Clearly, porous In_2O_3 nanostructures have exhibited excellent sensing properties, and therefore will be used in our proposed dual functional sensors for both UV light and H_2S sensing.

In this paper, porous In_2O_3 nanoparticles were prepared using a combined hydrothermal and calcination process. The dual functional sensors made of these porous nanoparticles were applied to detect both UV light and H_2S gas at room temperature, and ultra-high responses with low detection limits have been achieved.

2. Experimental procedures

2.1 Synthesis and characterization

$In(NO_3)_3$•$4.5H_2O$ of 0.762 g and glucose of 0.360 g were dissolved into 30 ml deionized water to obtain a fully transparent solution. Then, 1.2 ml of ethanolamine was added into the solution, and it was stirred for 30 minutes. Subsequently, the mixed solution was transferred into a Teflon lined stainless steel autoclave to hydrothermal react in an oven at 150 ^oC for 12 hours. After the hydrothermal reaction, a brown suspension was produced, and then centrifuged with a speed of 4000 r/min for 5 min to obtain a brown sediment. The sediment was washed using deionized water and ethanol, respectively, and then dried at 100 ^oC for 24 hours to obtain a brown InOOH powders. Finally, the InOOH powders were calcined at 500 ^oC for 2 hours to obtain yellow powders of In_2O_3.

X-ray diffraction (XRD, CuKα, 40kV/60mA, Rigaku D/max-2400) was conducted to analyze the In_2O_3 crystalline phases. Morphologies and crystallographic features were observed using a high resolution transmission electron microscope (HRTEM, JEM-

2200FS, Japan), attached with energy dispersive X-ray analysis (EDX) and selected area electron diffraction (SAED) analysis. UV-Vis absorption spectrum was recorded using a Shimadzu UV-2101 apparatus. X-ray photoelectron spectroscopy (XPS, Kratos Axis-Ultra DLD apparatus with Al Kα radiation) was conducted to analyze the chemical states of different elements on the sample surface. Nitrogen adsorption and desorption isotherm was obtained using a specific surface area/pore size analyzer of JW-BK122W (JWGB Sci. & Tech. Co. LTD). The specific surface area of samples was determined using the Brunauer–Emmett–Teller (BET) theory and the pore size distribution was calculated using Barrett–Joyner–Halenda (BJH) method.

2.2 Fabrication of the dual functional sensors

An aluminum oxide ceramic tube with gold electrodes on each end was used to fabricate the dual functional sensors for detection of both UV light and H_2S gas. The distance between the two gold electrodes was 2.0 mm. A pair of Pt wires were connected to the gold electrodes, and then connected to a Keithley 2400 Source Meter to measure the change of electric current. The In_2O_3 nanoparticles were uniformly dispersed in ethanol, and then were coated onto the outer surfaces of the ceramic tube to form a sensing film using a conventional dip coating method. Finally, the ceramic tube coated with the sensing film was calcined at 300 ^oC for 2 hours in air.

UV detection performance of the sensor was evaluated by measuring the change of photocurrent upon exposing the sensor to the UV light at room temperature of 25 ^oC. A portable UV analyzer (UV2A, Beijing SaiBaiAo Tech. Co. LTD, China, with a UV wavelength of 365 nm) was used as the source of UV radiation. The UV power intensity

was controlled by changing the distance to the sensor. A UVA light meter (LS126A, Shenzhen Linshang Tech. Co. Ltd., China) was placed side by side with the sensor to measure the intensity of UV radiation. The bias voltage used in the UV sensing tests was 1 V. For the H_2S gas sensing test, a Ni-Cr heating wire was placed in the ceramic tube and connected to a voltage-stabilized source to control the working temperature of gas sensors. The bias voltage used in the H_2S testing system was controlled to be 0.02 V. The sensor was placed inside a testing chamber with a volume of 2 liters. Different concentrations of the H_2S gas were precisely obtained by injecting different volumes of H_2S gas source. The relative humidity in testing process was fixed at 40%.

3. Results and discussion

3.1 Structure and morphology of samples

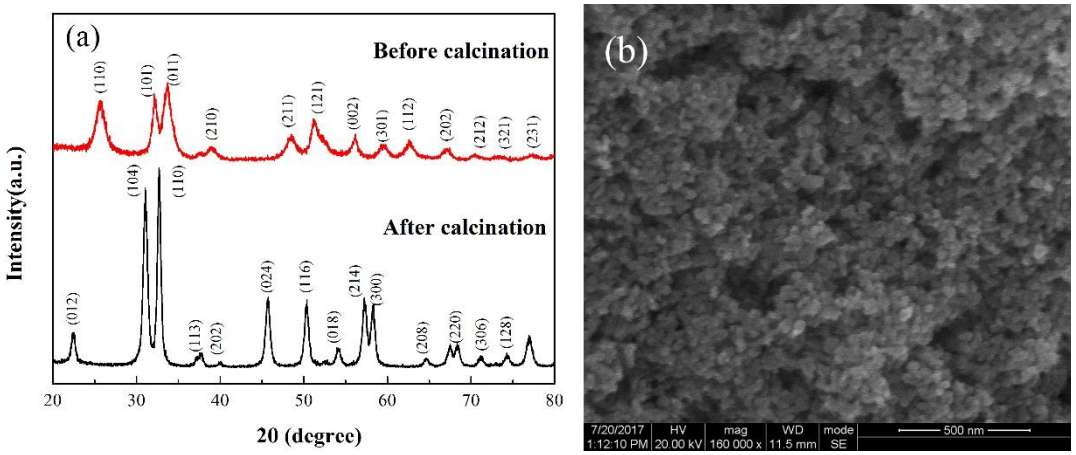

Figure 1. (a) XRD spectra of In_2O_3 samples before and after calcination, (b) SEM image of In_2O_3 sample

XRD spectra of the samples before and after calcination processes are shown in Figure 1a. The peaks in XRD pattern of the as-prepared powders before calcination process are corresponding to those of orthorhombic InOOH (lattice parameters a=5.23

Å, b=4.55 Å, c=3.26 Å, JCPDS NO. 71-2277), indicating that the sample obtained after the hydrothermal reaction is InOOH crystals. The XRD result of the powders calcined at 500 ^{o}C for two hours is shown in Figure 1a, and the peaks are perfectly indexed to the hexagonal phase of In_2O_3 with the lattice parameters of a=5.49 Å and c=14.52 Å (JCPDS card No.22-0336). This clearly indicates that the InOOH crystals have been completely transformed into the hexagonal In_2O_3 after the calcination treatment at 500 ^{o}C. Furthermore, the crystal sizes (L) of both the InOOH and In_2O_3 powders are estimated using the Scherrer formula:

$$L = K\lambda /(\beta \cos\theta) \quad (1)$$

where K is a constant of 0.89; θ is the diffracting angle; λ is the X-ray wavelength of 0.15406 nm, and β is the line width of peak at half maximum height. Based on the Scherrer equation, the average crystal sizes of InOOH and In_2O_3 powders are estimated to be about 6.8 nm and 19.9 nm, respectively. The growth of the crystal sizes during the transformation from InOOH to In_2O_3 is obvious during the calcination process. Figure 1b shows the SEM image of the In_2O_3 sample. It can be seen that the In_2O_3 nanoparticles are uniform, and the average diameter is about 20 nm, which agrees well with that obtained from the XRD analysis.

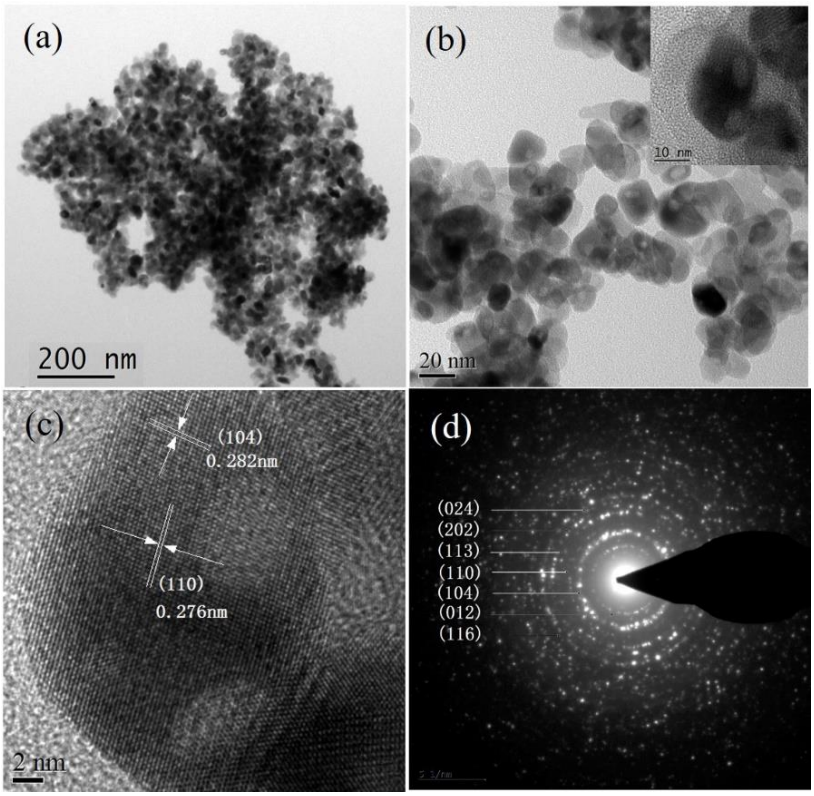

Figure 2. (a, b) TEM images of porous In_2O_3 nanoparticles, (c) HRTEM images and (d) SAED spectrum of porous In_2O_3 nanoparticles.

A low magnification TEM image of In_2O_3 sample is shown in Figure 2a. It reveals that the In_2O_3 nanoparticles have a uniform size distribution with an average diameter of ~20 nm, similar to that obtained from XRD analysis. From the high magnification TEM image shown in Figure 2b, many nano-pores can be observed on the surfaces of nanoparticles. The diameters of the nano-pores are in a range from 2.0 to 9.6 nm. These porous nanostructures can provide more surface areas and channels for the transport of gas molecules and facilitate the fast diffusion of H_2S towards the entire porous surface of the In_2O_3 nanostructure to achieve a quick response. They can also trap the UV light, which provides efficient ways to enhance light harvesting efficiency [21,22]. The HRTEM image (shown in Figure 2c) and SAED spectrum (shown in Figure 2d) prove

the good crystallinity of the In_2O_3 nanoparticles. The selected-area diffraction rings of (012), (104), (110), (113), (202), (024) and (116) in Figure 2d verify that the phases of samples are hexagonal In_2O_3, which agrees with the results of crystal structural analysis from XRD. In the HRTEM image shown in Figure 2c, the planes with spaces of 0.276 nm and 0.282 nm are corresponding to (110) and (104) planes of the In_2O_3 crystals.

In the synthesis process, ethanolamine is hydrolyzed to generate NH_3 molecules. The OH^- ions are then produced by the hydrolysis of these NH_3 molecules. These reactions can be written using the following equations:

$$HO(CH_2)_2NH_2 + H_2O \rightarrow HO(CH_2)_2OH + NH_3 \quad (2)$$

$$NH_3 + H_2O \rightarrow NH_4^+ + OH^- \quad (3)$$

In the hydrothermal reaction, the In^{3+} ions react with OH^- to form InOOH nanoparticles, which can be written in equation (4). At the same time, some NH_3 gas bubbles are entrapped inside the InOOH nanoparticles. During the calcination treatment at 500 ^oC, the entrapped NH_3 gas bubbles are decomposed and nano-pores are formed on the surfaces of nanoparticles (see Figure 2b), and the InOOH nanoparticles are recrystallized and transformed into hexagonal phases of In_2O_3, as listed in equation (5).

$$In^{3+} + 3OH^- \rightarrow InOOH + H_2O \quad (4)$$

$$2InOOH \rightarrow h\text{-}In_2O_3 + H_2O \quad (5)$$

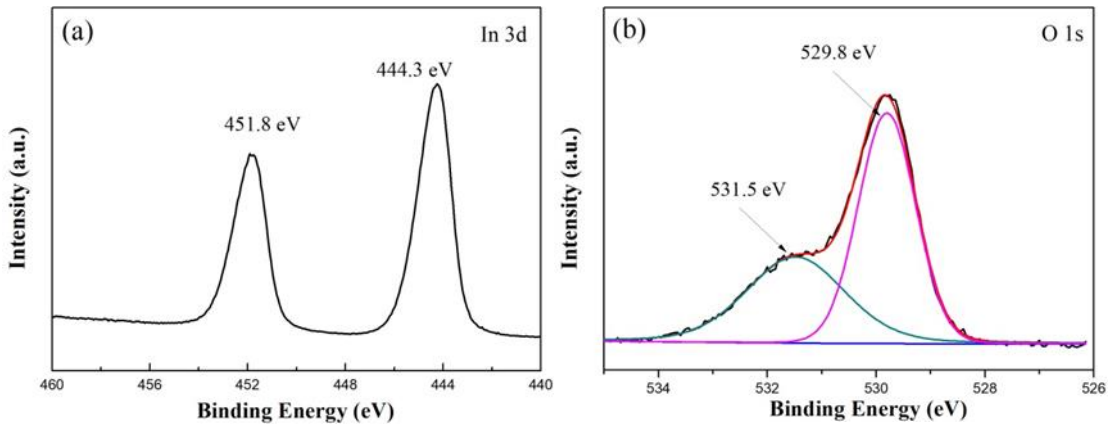

Figure 3. (a) In 3d and (b) O 1s XPS spectra of porous In_2O_3 nanoparticles

The In 3d and O 1s XPS spectra of the porous In_2O_3 nanoparticles are shown in Figure 3. The peaks at 444.3 eV and 451.8 eV in Figure 3a of the In 3d spectrum are assigned to the characteristic spin-orbit splits of In $3d_{5/2}$ and In $3d_{3/2}$ signals, respectively, which are in a good agreement with the characteristic chemical valence of In^{3+} ions [27]. The O1s spectrum in Figure 3b shows two obvious peaks at 529.8 and 531.5 eV, respectively. The peak centered at 529.8 eV is corresponding to lattice oxygen in In_2O_3, and the peak centered at 531.5 eV is corresponding to adsorbed oxygens on the surface of porous In_2O_3 nanoparticles. Furthermore, based on the calculated integral proportion of XPS peaks at 529.8 and 531.5 eV, the ratio of the lattice oxygens and adsorbed oxygen species is estimated to be 41.3:58.7. This indicates that there are many adsorbed oxygen species on the surface of porous In_2O_3 nanoparticles. The existence of nano-pores on the surface of In_2O_3 nanoparticles generates more active sites on the In_2O_3 nanoparticles to adsorb more oxygen species, which is beneficial to the sensing performance [21,22].

3.2 UV and H_2S sensing properties

3.2.1 UV sensing results

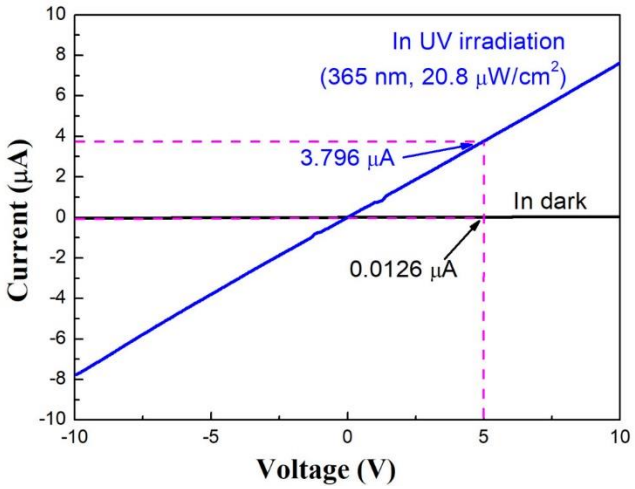

Figure 4. I-V curves of the sensor based on porous In_2O_3 nanoparticles measured in dark and in UV irradiation (λ = 365 nm, power density = 20.8 μW/cm^2) respectively.

The current-voltage (I-V) curves of the sensor based on porous In_2O_3 nanoparticles are shown in Figure 4, which were measured in both dark and UV irradiation (with a wavelength of 365 nm and a power density of 20.8 μW/cm^2), respectively. Obviously, both the I-V curves show ideal linear characteristics, indicating that the sensor has a good ohmic contact in both dark and UV irradiations. Furthermore, the current of the sensor is very low in the dark (e.g., 0.0126 μA at the voltage of 5V). Whereas, under the UV irradiation with a low power density of 20.8 μW/cm^2, the photocurrent is as large as 3.796 μA at the voltage of 5V. This results in an on/off ratio of 301.3 times, indicating a good response of UV detection.

Figure 5a shows the response/recovery curves of the sensor based on porous In_2O_3 nanoparticles at different UV irradiation intensities at room temperature. When the sensor is exposed to the UV irradiation, the photocurrent of sensors is increased immediately, and then it is saturated before reaching to a maximum value. After the UV light is turned off, the photocurrent is gradually decreased to its initial value. This

indicates that the UV light sensor has not only a high response, but also a good reversibility.

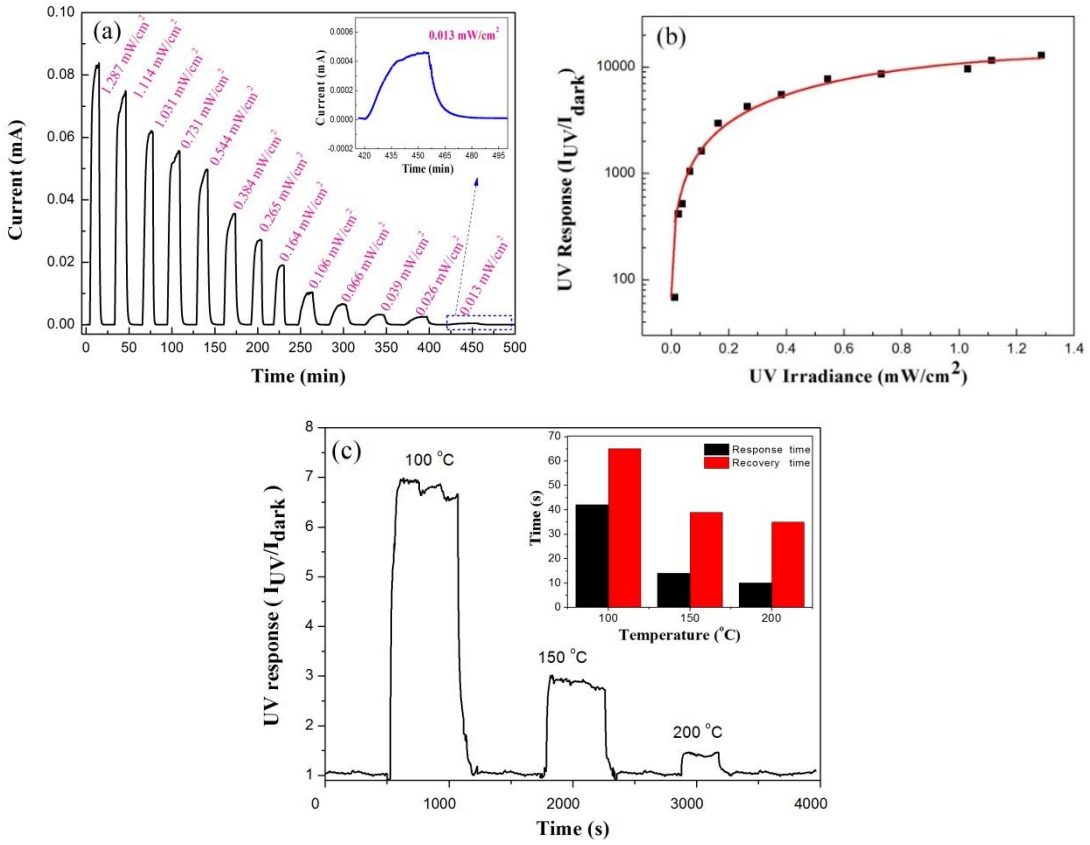

Figure 5. (a) Response/recovery curves of porous In_2O_3 nanoparticles based sensor at different UV (365 nm) irradiation intensities at room temperature, (b) the relationship between response with UV (365 nm) power intensity, (c) response/recovery curves of the sensor at higher working temperature to 0.544 mW/cm^2 UV intensity light (the inset is histogram of the response/recovery times).

The UV response (R_{UV}) of the sensor is defined as the ratio of photocurrent (I_{UV}) to the dark current (I_{dark}), i.e., $R_{UV} = I_{UV}/I_{dark}$.[28] The response data are calculated and the results are shown in Figure 5b, in which the UV response increases with the increase of UV power intensity. Results show that the UV sensor based on porous In_2O_3 nanoparticles exhibits a large response to the UV light (with a wavelength of 365 nm)

and a low detection limit. The response is as large as 12886.0 when the sensor is tested with the UV power intensity of 1.287 mW/cm^2. When the intensity of UV light is changed to a low intensity of 0.013 mW/cm^2, the response is still as large as 68.0. Compared with other reported UV sensors based on different metal oxide materials in the literature, such as WO_3 [29], SnO_2 [30], TiO_2 [31] and ZnO [32, 33], the UV sensors based on porous In_2O_3 nanoparticles in this study have better sensing performance (i.e., the response) than most UV sensors at room temperature.

As shown in Figure 5a, the response/recovery times of the UV sensors are is longer than 200 s. To reduce the response and recovery time, effect of working temperature on the sensor responses is investigated. The response/recovery curves of the sensor at higher working temperatures with a fixed UV light intensity of 0.544 mW/cm^2 are shown in the Figure 5c. It is found that increase of working temperatures can significantly shorten the response/recovery time to less than 65 s. However, the UV responses of the sensor were found to decrease with the increase of working temperature. Therefore, reducing the response/recovery time of the UV sensor without sacrificing the sensor's responses will be our next research target.

3.2.2 H_2S gas sensing performance

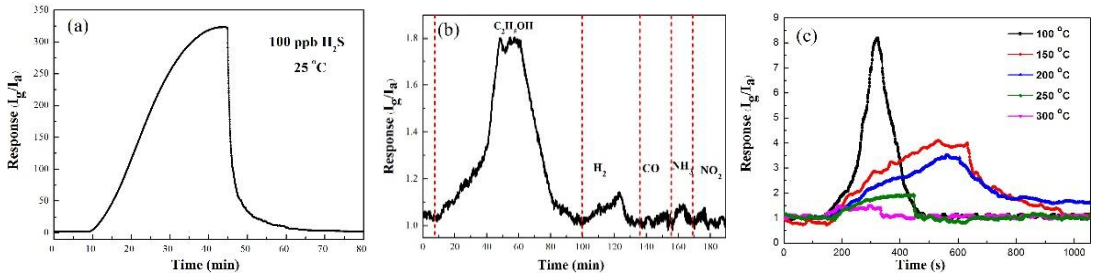

Figure 6. (a) Response of the porous In_2O_3 nanoparticles based sensor to 100 ppb of H_2S at room temperature, (b) responses of the sensor to other gases (C_2H_5OH, H_2, CO,

NH_3 and NO_2) with 10 ppm concentration at room temperature, (c) responses of the sensor to 100 ppb of H_2S at different working temperatures.

To analyze the selectivity of In_2O_3 based sensor to different gases (a key factor for the sensor to avoid the false alarms due to influence of other gases) [34], the responses of the sensor to 100 ppb of H_2S and other different gases of C_2H_5OH, H_2, CO, NH_3 and NO_2 with 10 ppm concentration are measured at room temperature, and the results are shown in Figures 6a and 6b. The gas response of the sensor is defined as: $R_{gas} = I_{gas}/I_{air}$, where I_{air} and I_{gas} are the current value of the sensor measured in air and the target gas, respectively. From Figure 6a, the porous In_2O_3 nanoparticles based sensor shows a high response of 323.3 for 100 ppb of H_2S. However, the responses of the sensor to other gases are relatively small, which are generally smaller than 1.1 even with a high concentration of 10 ppm of H_2, CO, NH_3 and NO_2, respectively. For 10 ppm of C_2H_5OH, the porous In_2O_3 nanoparticles based sensor shows an obvious response, but the response is only 1.8. Therefore, compared with that for the H_2S, the responses of the sensor to other gases are almost negligible. This clearly indicates that the sensor based on the porous In_2O_3 nanoparticles has a good selectivity for the detection of H_2S operated at room temperature.

The low working temperature is another important factor for the successful application of the gas sensor [35,36]. To find the optimal working temperature, the responses of the sensor made of porous In_2O_3 nanoparticles to 100 ppb H_2S have been measured at different working temperatures. The obtained responses of the sensor are shown in Figures 6c. With the increase of working temperature, the responses of the

sensor are decreased. When the working temperatures are above 100 ^{o}C, the response value are lower than 8.5. At room temperature (i.e., 25 ^{o}C), the sensor exhibited the highest response value of 323.3 to 100 ppb H_2S. Therefore, the optimal working temperature for the sensor is room temperature.

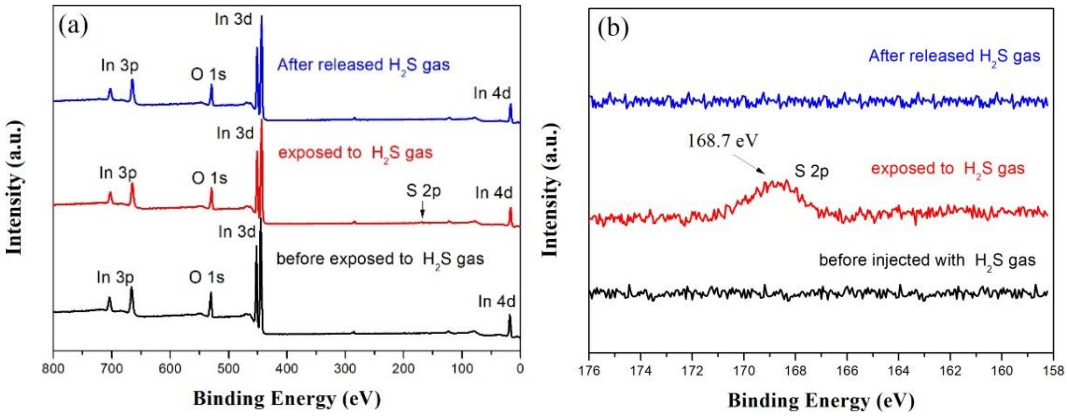

Figure 7. (a) XPS survey spectra and (b) high resolution S 2p XPS spectra of porous In_2O_3 nanoparticles before exposed to H_2S, when exposed to H_2S and after released H_2S gas, respectively.

To investigate the effect of H_2S on the surface chemical states of porous In_2O_3 nanoparticles during the testing process at room temperature, the XPS spectra of porous In_2O_3 nanoparticles before exposed to H_2S, when exposed to H_2S and after released H_2S gas were measured, respectively. Figure 7a shows the survey spectra of In_2O_3 and Figure 7b shows the corresponding high resolution XPS spectra of S 2p. When the porous In_2O_3 nanoparticles are exposed to H_2S, It can be seen that a signal of S element appears in the XPS spectrum. The peak at 168.7 eV is assigned to H_2S molecules, which are absorbed on the surface of In_2O_3. However, after the H_2S gas is released from the sensor, no S element is found in the XPS spectra, which is the same as the result before the porous In_2O_3 nanoparticles is exposed to H_2S. This clearly proved that there is no

contamination of the sensitive surface with sulfur after the H_2S gas was released.

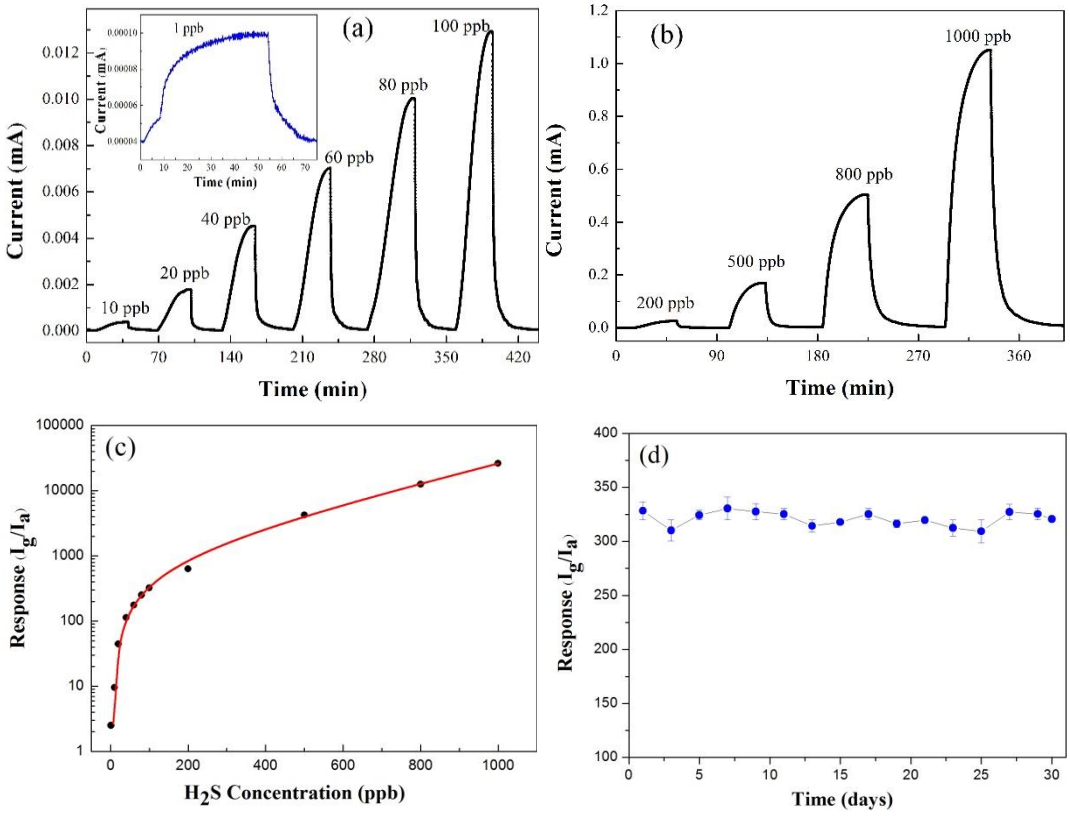

Figure 8. Response/recovery curves of the porous In_2O_3 nanoparticles based sensor to different H_2S concentrations at room temperature: (a) 1 ppb ~ 100 ppb, (b) 200 ppb ~ 1000 ppb, (c) responses of the porous In_2O_3 nanoparticles based sensor for different H_2S concentration at room temperature, (d) stability of the sensor to 100 ppb H_2S gas in a month tested at room temperature.

Figure 8a and 8b shows the response/recovery curves of the sensor based on the porous In_2O_3 nanoparticles exposed to different H_2S concentrations at room temperature. With the introduction of H_2S into the testing chamber, the electric current of sensor is increased but then gradually saturated, reaching to a maximum value. When the H_2S is replaced by air, the electric current of the sensor is decreased to its initial value before introducing the H_2S gas. Therefore, at room temperature, the

response/recovery curves of the sensor showed a good reversibility.

Figure 8c shows the response values of the porous In_2O_3 nanoparticles based sensor to different H_2S concentrations at room temperature. An exponential function relationship can be found between the response (R) data and concentration of H_2S (C_{H2S}), which can be written using the following equation:

$$R = 880.33 \times \exp(C_{H2S}/291.67) - 908.74 \quad (7)$$

When the H_2S concentration is increased, the response is increased accordingly. The sensitivities of the sensor are significantly ultra-high, e.g., for the 1 ppm of H_2S, the measured response is 26268.5. Table 1 lists the literature-reported sensing properties of H_2S sensors which are made using different metal oxide materials including In_2O_3. Compared with other types of H_2S gas sensors, the response of the sensor based on porous In_2O_3 nanoparticles in this study has the largest reported value so far. Based on the results shown in Figure 8c, even with a low H_2S concentration of 1 ppb, the sensor still shows apparent signals with a response of 2.5, indicating that the porous In_2O_3 nanoparticles based sensor has a low detection limit down to 1 ppb. As far as we have searched in the literature, the H_2S detection limit of 1 ppb at room temperature in this study is also the lowest reported value for the H_2S detection at room temperature using various metal oxide based gas sensors (as listed in table 1).

Table 1. Sensing properties of H_2S sensors based on different metal oxide materials.

Materials	Structure	Working Temp.	Conc.	Response	Detection limit	Ref.
ZnO	nanorod	190 °C	100 ppm	34.8	10 ppm	[37]
Mo-ZnO	nanowire	300 °C	5 ppm	14.11	0.2 ppm	[38]
α-Fe_2O_3	porous nanoparticle	25 °C	100 ppm	38.4	50 ppb	[21]
NiO	porous nanowall	92 °C	50 ppm	20.6	1 ppb	[39]
SnO_2	olive nanocrystal	240 °C	20 ppm	200	0.5 ppm	[40]
SnO_2	multi-tube array	25 °C	100 ppm	5.21	5 ppm	[41]
SnO_2	sensing film	350 °C	10 ppm	2274	0.25ppm	[42]
SnO_2	quantum wire	25 °C	50 ppm	33	10 ppm	[43]
CuO	Porous nanosheet	25 °C	1 ppm	9.8	10 ppb	[10]
CuO	nanowires	180 °C	0.1 ppm	23.7	2.5 ppb	[44]
ZnO/SnO_2	nanosphere	100 °C	10 ppm	99.6	10 ppb	[45]
$ZnFe_2O_4$	porous nanosheet	85 °C	5 ppm	123	500 ppb	[46]
In_2O_3/WO_3	nanoparticle	150 °C	10 ppm	143	0.5 ppm	[47]
Mg-In_2O_3	nanotube	130 °C	10 ppm	1959.77	–	[48]
CuO-In_2O_3	nanofiber	150 °C	5 ppm	9170	0.4 ppm	[49]
V-In_2O_3	nanofiber	90 °C	50 ppm	14	1 ppm	[50]
Eu-In_2O_3	nanobelt	260 °C	100 ppm	5.74	5 ppm	[51]
In_2O_3	porous film	300 °C	50 ppm	30	1 ppm	[19]
In_2O_3	Porous nanoparticle	25 °C	1 ppm	26268.5	1 ppb	This work

To investigate the stability of the H_2S sensor based on porous In_2O_3 nanoparticles, the response values of the sensor to 100 ppb of H_2S have been measured in every two-day period within one month, and the response results are shown in Figure 8d. The response values are found to be relatively stable at 320.1 within one month, and the largest deviation of response value is lower than 3.3%, indicating the good stability of the sensor in one month. Therefore, from the above results, it can be confirmed that the sensor based on porous In_2O_3 nanoparticles has not only a good selectivity, a high response and a low detection limit, but also a good stability to H_2S at room temperature.

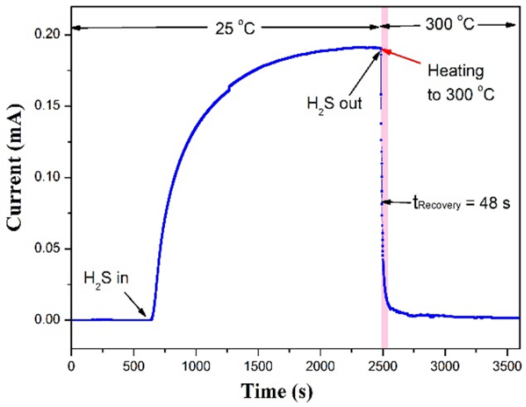

Figure 9. Dynamic response/recovery curve of the sensor based on porous In_2O_3 nanoparticles for 500 ppb H_2S at a recovery temperature of 300 ^oC.

From the response curves of the sensors shown in Figure 8a and 8b, the response and recovery times of the sensor based on porous In_2O_3 nanoparticles are relatively long for H_2S gas at room temperature. The reason for this might be due to the nanoporous structures, in which the gas molecules need to gradually diffuse into these. However, it can be found that after the H_2S gas is injected, at a very short time, the sensor can actually reach very high response values. For examples, when injected with 500 ppb or 1000 ppb H_2S after 120 s, the sensor already shows high response values of 565.8 and 3659.7, respectively, although the time to reach to 90% of their maximum values is much longer. For the recovery times, it can be significantly reduced by heating the substrate to 300 ^oC during the recovery process. For example, from the dynamic response/recovery curve of the sensor for 500 ppb H_2S at a recovery temperature of 300 ^oC in Figure 9, it can be found that, after reaching its highest electric current (the response value is 4526.7) at room temperature, the recovery time was only 48 s by heating the sensor to 300 ^oC during the recovery process. Therefore, we can conclude that the recovery time of the sensor based on porous In_2O_3 nanoparticles can be

significantly decreased by heating the substrate to 300 °C during the recovery process.

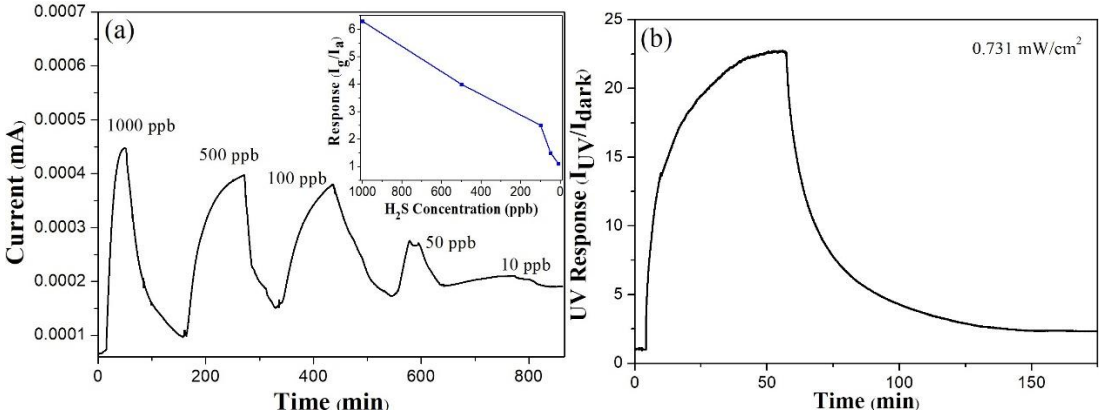

Figure 10. (a) Response/recovery curves for H_2S and (b) response/recovery curve for UV (0.731 μW/cm^2) of the sensor based on commercial In_2O_3 powder (99.99%, 20 nm, Macklin Biochemical Co., Ltd.) at room temperature. (The inset in Fig. 10a is response values to H_2S with different concentrations).

In order to highlight the improvement of sensing performance of porous In_2O_3 nanoparticles in this study, we measured the sensing properties of high purity commercial In_2O_3 nanoparticles (99.99%) with an average nanoparticle size of 20 nm, which is purchased from Macklin Biochemical Co., Ltd. The response/recovery curves of the commercial In_2O_3 based sensor for H_2S at room temperature are shown in Figure 10a. It can be seen that the response value of commercial In_2O_3 nanoparticles to 1 ppm H_2S is only 6.3, which is much lower than that of the porous In_2O_3 nanoparticles in this study (26268.5 for 1 ppm H_2S). And the detection limit of commercial In_2O_3 nanoparticles is 10 ppb, which is larger than that of the porous In_2O_3 nanoparticles (1 ppb). In addition, the UV sensing performance of the commercial In_2O_3 at room temperature are also measured and shown in Figure 10b. The response value to UV with a power density of 0.731 μW/cm^2 is 22.7. However, the response value of porous

In_2O_3 nanoparticles based sensor is as high as 8585.0 for UV with 0.731 μW/cm^2. Therefore, the porous In_2O_3 nanoparticles based sensor in this study has better sensing performance for UV and H_2S than the commercial In_2O_3 nanoparticles.

3.2.3 Sensing mechanisms

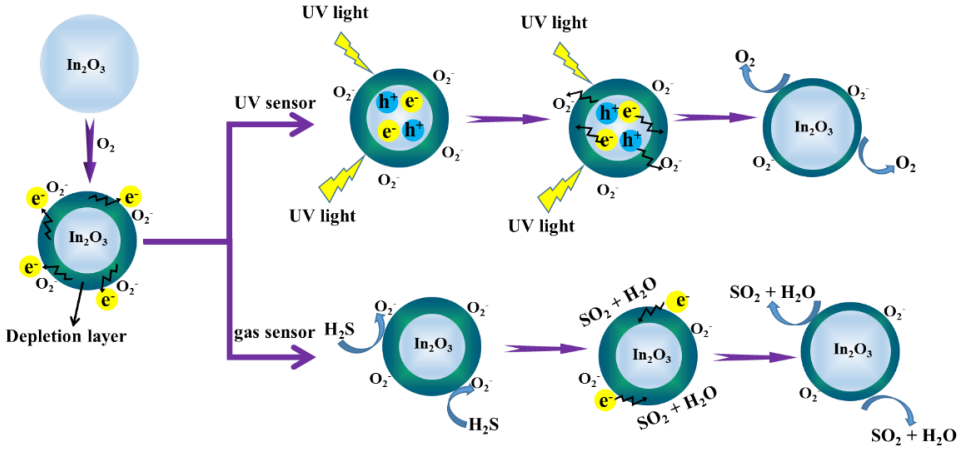

Figure 11. Schematic diagram showing the sensing mechanisms to UV and H_2S for the dual functional sensors based on porous In_2O_3 nanoparticles

Similar to most of metal oxide based sensors, the sensing mechanism of the sensor in this study is based on the conductivity changes of the sensing material (i.e., the porous In_2O_3 nanoparticles) when it is exposed to UV light or H_2S gas [52]. Figure 11 presents a schematic diagram of the sensing mechanisms to both UV light and H_2S gas for the dual functional sensor based on the porous In_2O_3 nanoparticles. In air, the oxygen molecule will be adsorbed on the surface of the sensing materials of metal oxides. At room temperature, the chemisorption of oxygen molecules will extract free electrons and form oxygen species based on the following reaction equation:[53,54]

$$O_{2(g)} + e^- \rightarrow O_2^-{}_{(ads)} \quad (8)$$

Because of the consumption of free electrons in this reaction process, a deletion layer

is formed on the surfaces of the In_2O_3 nanoparticles [55]. Due to the formation of this deletion layer, the conductivity of the In_2O_3 based sensor is decreased, and so does the current of the In_2O_3 sensor. XPS analysis in Figure 3 proves that there are many adsorbed oxygen species on the surface of porous In_2O_3 nanoparticles. The porous nanostructures of the In_2O_3 should have more active sites on their surfaces for the formation of abundant O_2^- ions, which can trigger more surface sensing reactions with UV light or H_2S gas to achieve high sensitivity [21].

When the In_2O_3 based sensor is exposed to the UV light, the energy of photon is absorbed by the In_2O_3 nanostructure, and then the electron–hole pairs will be generated quickly. At the same time, the adsorbed oxygen ions will capture the free holes and transform to oxygen molecule based on the following equations:[2,3]

$$h\nu \rightarrow e^- + h^+ \quad (9)$$

$$O_{2(ads)}^- + h^+ \rightarrow O_2 \quad (10)$$

As a result, the unpaired electrons will accumulate, thus leading to the reduction of the deletion layers. This process will result in an increase of the conductivity of In_2O_3 nanoparticles, and thus an increase of photocurrent of the In_2O_3 based sensor. The nano-pores on the surfaces of In_2O_3 nanoparticles can trap more UV light, which increases its response and thus provides an efficient way to enhance its light harvesting efficiency [56].

When the sensor is exposed to H_2S gas, the H_2S molecules will be absorbed on the surfaces of the In_2O_3 nanoparticles and react with the O_2^- ions to release electrons as follows: [21,46]

$$2H_2S_{(g)} + 3O_2^-{}_{(ads)} \leftrightarrow 2H_2O_{(g)} + 2SO_{2(g)} + 3e^- \quad (11)$$

The H_2S molecules act as electron donors during the process, resulting in the reduction of the deletion layers and also the increase of the conductivity of the In_2O_3 layer. This will result in an increase of the current of the sensor. The special porous nanostructures of sensing materials provide an efficient way to facilitate the diffusion of H_2S towards the entire porous surface of the In_2O_3 nanostructure, resulting in a high response of the sensor [56].After the H_2S gas is replaced by the air, the O_2 molecules will be re-adsorbed on the In_2O_3 surface and trap free electrons to form O_2^- ions again. As a result, the electric current of the sensor returns to its initial value before introducing the H_2S gas.

For the H_2S sensing, in addition to the adsorption and desorption sensing mechanism, Xu et al.[57] and Wang et al.[19] proposed another sensing mechanism for the In_2O_3 materials based on thermodynamic analysis. It is proposed that a sulfuration process can happen on the surfaces of In_2O_3 when they are exposed to H_2S gas at room temperature, and the reaction equation can be listed below:[19,57]

$$In_2O_{3(s)} + 3H_2S_{(g)} \rightarrow In_2S_{3(s)} + 3H_2O_{(g)} \quad (12)$$

Because the change of Gibbs free energies is −161.7 kJ mol^{-1} at 25 °C for the above chemical reaction, the formation of In_2S_3 from In_2O_3 is triggered spontaneously and thermodynamically [57]. As a result, a layer of In_2S_3 film can form on the surfaces of In_2O_3 nanoparticles. Due to the good conductivity of In_2S_3, the electrical current of the sensor will be remarkably increased thus resulting in a large response to the H_2S gas. Therefore, we believe that the ultra-high response of the porous In_2O_3 nanoparticles

based sensor to the H_2S gas is not only due to the oxidation process by surface adsorption of oxygen, but also due to the formation of the In_2S_3 by the sulfuration mechanism as mentioned above.

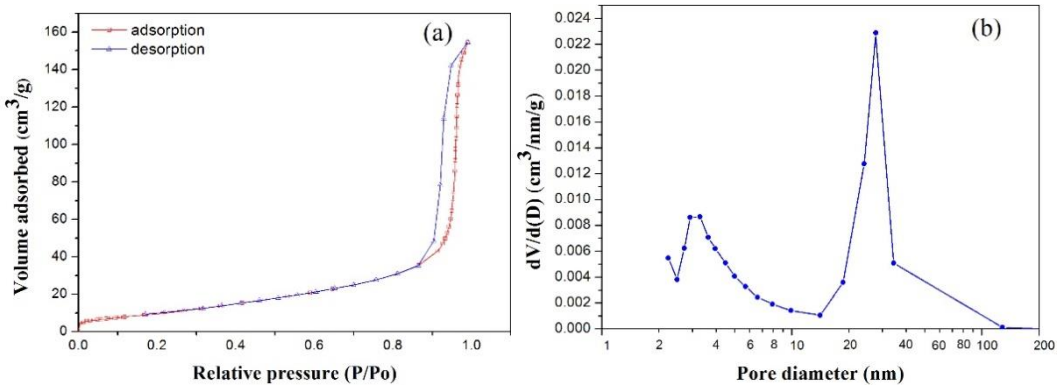

Figure 12. (a) N_2 adsorption–desorption isotherms and (b) pore-size distribution of the porous In_2O_3 nanoparticles.

To further explain the large responses of the dual functional sensors based on porous In_2O_3 nanoparticles, the specific surface areas and porosity have been measured. The nitrogen gas adsorption-desorption isotherms of the In_2O_3 particles are shown in Figure 12a. There is a hysteresis loop observed with the relative pressure changed from 0.8 to 1.0 (P/P_0). Therefore, the In_2O_3 nanoparticles exhibit a type IV isotherm, i.e., there are mesopores existed in the In_2O_3 nanoparticles [24,25].The pore size distribution of the porous In_2O_3 nanoparticles calculated using the BJH method is shown in Figure 12b. It can be seen that there are two types of pore size distributions, i.e., the first one is from 2.4 to 9.9 nm with a center average value of 3.3 nm, and the second one is from 13.3 to 33.8 nm with a center average value of 27.3 nm. The former pore size distribution is attributed to the pores within the In_2O_3 nanoparticles, and the latter one is attributed to the pores formed within the aggregates of many nanoparticles. The BET specific

surface areas and the pore volumes of the porous In_2O_3 nanoparticles are measured to be about 60.6 m^2/g and 0.24 cm^3/g, respectively. Results clearly show that the prepared In_2O_3 nanoparticles possess a mesoporous structure with large surface areas and large pore volumes. We believe that the above mesoporous nano-particulate structures are beneficial for gas absorption/diffusion and could provide plenty of active sites for both UV and gas sensing reactions [45]. Accordingly, the dual functional sensors based on porous In_2O_3 nanoparticles exhibit high responses to both UV light and H_2S gas.

4. Conclusions

Porous In_2O_3 nanoparticles with large surface areas and pore volumes were synthesized using hydrothermal and calcination process. Dual-function sensors were fabricated using these porous nanoparticles to detect both ultraviolet (UV) light and H_2S gas at room temperature. The mesoporous structures of In_2O_3 nanoparticles could provide plenty of active sites for both UV and H2S sensing reactions. Results showed that these dual-function sensors exhibited ultra-high responses and low detection limits to both UV light (365 nm) and H_2S gas at room temperature. In brief, the dual-function sensors based on hexagonal phase porous In_2O_3 nanoparticles have promising application in UV monitoring and H_2S detection.

ACKNOWLEDGMENTS

Funding supports from UK Engineering Physics and Science Research Council (EPSRC EP/P018998/1), Newton Mobility Grant (IE161019) through Royal Society and NFSC, and Royal academy of Engineering UK-Research Exchange with China and

India are acknowledged.

REFERENCE

[1] S.K. Shaikh, V.V. Ganbavle, S.I. Inamdar, K.Y. Rajpure, Multifunctional zinc oxide thin films for high-performance UV photodetectors and nitrogen dioxide gas sensors, RSC Adv. 6 (2016) 25641–25650.
[2] Y. Luo, C. Zhang, Pt-activated TiO_2 -MoS_2 nanocomposites for H_2 detection at low temperature, J. Alloy. Compd., 747 (2018) 550-557.
[3] D. Kim, G. Shin, J. Yoon, D. Jang, S.J. Lee, G. Zi, J.S. Ha, High performance stretchable UV sensor arrays of SnO_2 nanowires, Nanotechnology 24 (2013).
[4] P.S. Shewale, S.H. Lee, Y.S. Yu, UV sensitive pulsed laser deposited ZnO thin films: Influence of growth temperature, J. Alloy. Compd., 744 (2018) 849-858.
[5] P.S. Kolhe, A.B. Shinde, S.G. Kulkarni, N. Maiti, P.M. Koinkar, K.M. Sonawane, Gas sensing performance of Al doped ZnO thin film for H_2S detection, J. Alloy. Compd., 748 (2018) 6-11.
[6] Z. Li, Z. Lin, N. Wang, Y. Huang, J. Wang, W. Liu, Y. Fu, Z. Wang, Facile synthesis of α-Fe_2O_3 micro-ellipsoids by surfactant-free hydrothermal method for sub-ppm level H_2S detection, Mater. Des. 110 (2016) 532-539.
[7] C. Cao, C. Hu, X. Wang, S. Wang, Y. Tian, H. Zhang, UV sensor based on TiO_2 nanorod arrays on FTO thin film, Sens. Actuators B 156 (2011) 114–119.
[8] R. Lontio Fomekong, H.M. Tedjieukeng Kamta, J. Ngolui Lambi, D. Lahem, P. Eloy, M. Debliquy, A. Delcorte, A sub-ppm level formaldehyde gas sensor based on Zn-doped NiO prepared by a co-precipitation route, J. Alloy. Compd., 731 (2018) 1188-1196.
[9] S.C. Zhang, Y.W. Huang, Z. Kuang, S.Y. Wang, W.L. Song, D.Y. Ao, W. Liu, Z.J. Li, Solvothermal synthesized In_2O_3 nanoparticles for ppb level H_2S detection, Nanosci. Nanotech. Lett. 7 (2015) 455–461.
[10] Z. Li, N. Wang, Z. Lin, J. Wang, W. Liu, K. Sun, Y.Q. Fu, Z. Wang, Room-temperature high-performance H_2S Sensor Based on porous CuO nanosheets prepared by hydrothermal method, ACS Appl. Mater. Inter. 8 (2016) 20962–20968.
[11] K. Yao, D. Caruntu, Z. Zeng, J. Chen, C.J. O'Connor, W. Zhou, Parts per billion-level H_2S detection at room temperature based on self-assembled In_2O_3 nanoparticles, J. Phys. Chem. C 113 (2009) 14812–14817.
[12] Q. Qi, P.P. Wang, J. Zhao, L.L. Feng, L.J. Zhou, R.F. Xuan, Y.P. Liu, G.D. Li, SnO_2 nanoparticle-coated In_2O_3 nanofibers with improved NH_3 sensing properties, Sens. Actuators B 194 (2014) 440–446.
[13] S.J. Kim, I.S. Hwang, Y.C. Kang, J.H. Lee, Design of selective gas sensors using additive-loaded In_2O_3 hollow spheres prepared by combinatorial hydrothermal reactions, Sensors-Basel 11 (2011) 10603–10614.
[14] X. Wang, M. Zhang, J. Liu, T. Luo, Y. Qian, Shape- and phase-controlled synthesis of In_2O_3 with various morphologies and their gas-sensing properties, Sens. Actuators B 137 (2009) 103–110.
[15] A. Shanmugasundaram, B. Ramireddy, P. Basak, S.V. Manorama, S. Srinath, Hierarchical $In(OH)_3$ as a precursor to mesoporous In_2O_3 nanocubes: a facile synthesis route, mechanism of self-assembly, and enhanced sensing response toward hydrogen, J. Phys. Chem. C 118 (2014) 6909–

6921.
[16] F. Gong, H. Liu, C. Liu, Y. Gong, Y. Zhang, E. Meng, F. Li, 3D hierarchical In_2O_3 nanoarchitectures consisting of nanocuboids and nanosheets for chemical sensors with enhanced performances, Mater. Lett. 163 (2016) 236–239.
[17] L. Guo, X. Shen, G. Zhu, K. Chen, Preparation and gas-sensing performance of In_2O_3 porous nanoplatelets, Sens. Actuators B 155 (2011) 752–758.
[18] A. Montazeri, F. Jamali-Sheini, Enhanced ethanol gas-sensing performance of Pb-doped In_2O_3 nanostructures prepared by sonochemical method, Sens. Actuators B 242 (2017) 778–791.
[19] Y. Wang, G. Duan, Y. Zhu, H. Zhang, Z. Xu, Z. Dai, W. Cai, Room temperature H_2S gas sensing properties of In_2O_3 micro/nanostructured porous thin film and hydrolyzation-induced enhanced sensing mechanism, Sens. Actuators B 228 (2016) 74–84.
[20] V.D. Kapse, S.A. Ghosh, G.N. Chaudhari, F.C. Raghuwanshi, Nanocrystalline In_2O_3-based H_2S sensors operable at low temperatures, Talanta 76 (2008) 610–616.
[21] J. Deng, J. Ma, L. Mei, Y. Tang, Y. Chen, T. Lv, Z. Xu, T. Wang, Porous alpha-Fe_2O_3 nanosphere-based H_2S sensor with fast response, high selectivity and enhanced sensitivity, J. Mater. Chem. A 1 (2013) 12400–12403.
[22] Y. Huang, W. Chen, S. Zhang, Z. Kuang, D. Ao, N.R. Alkurd, W. Zhou, W. Liu, W. Shen, Z. Li, A high performance hydrogen sulfide gas sensor based on porous alpha-Fe_2O_3 operates at room-temperature, Appl. Surf. Sci. 351 (2015) 1025–1033.
[23] X. Sun, H. Hao, H. Ji, X. Li, S. Cai, C. Zheng, Nanocasting synthesis of In_2O_3 with appropriate mesostructured ordering and enhanced gas-sensing property, ACS Appl. Mater. Inter. 6 (2014) 401–409.
[24] X. Wang, J. Su, H. Chen, G.D. Li, Z. Shi, H. Zou, X. Zou, Ultrathin In_2O_3 nanosheets with uniform mesopores for highly sensitive nitric oxide detection, ACS Appl. Mater. Inter. 9 (2017) 16335–16342.
[25] S. Zhang, P. Song, J. Li, J. Zhang, Z. Yang, Q. Wang, Facile approach to prepare hierarchical Au-loaded In_2O_3 porous nanocubes and their enhanced sensing performance towards formaldehyde, Sens. Actuators B 241 (2017) 1130–1138.
[26] T. Hyodo, E. Fujii, K. Ishida, T. Ueda, Y. Shimizu, Microstructural control of porous In_2O_3 powders prepared by ultrasonic-spray pyrolysis employing self-synthesized polymethylmethacrylate microspheres as a template and their NO_2-sensing properties, Sens. Actuators B 244 (2017) 992–1003.
[27] W. Yin, D.V. Esposito, S. Yang, C. Ni, J.G. Chen, G. Zhao, Z. Zhang, C. Hu, M. Cao, B. Wei, Controlling novel red-light emissions by doping In_2O_3 nano/microstructures with interstitial nitrogen, J. Phys. Chem. C 114 (2010) 13234–13240.
[28] H. Zhang, Y. Hu, Z. Wang, Z. Fang, L.-M. Peng, Performance boosting of flexible ZnO UV sensors with rational designed absorbing antireflection layer and humectant encapsulation, ACS Appl. Mater. Inter. 8 (2016) 381–389.
[29] Y.M. Juan, S.J. Chang, H.T. Hsueh, T.C. Chen, S.W. Huang, Y.H. Lee, T.J. Hsueh, C.L. Wu, Self-powered hybrid humidity sensor and dual-band UV photodetector fabricated on back-contact photovoltaic cell, Sens. Actuators B 219 (2015) 43–49.
[30] M. Augustin, M. Sommer, V.V. Sysoev, UV-VIS sensor system based on SnO_2 nanowires, Sens. Actuators A 210 (2014) 205–208.
[31] W.S. Lee, Y.S. Park, Y.K. Cho, Hierarchically structured suspended TiO_2 nanofibers for use in

UV and pH sensor devices, ACS Appl. Mater. Inter. 6 (2014) 12189–12195.
[32] D. Gedamu, I. Paulowicz, S. Kaps, O. Lupan, S. Wille, G. Haidarschin, Y.K. Mishra, R. Adelung, Rapid fabrication technique for interpenetrated ZnO nanotetrapod networks for fast UV sensors, Adv. Mater. 26 (2014) 1541–1550.
[33] S.F. Akhtarianfar, A. Khayatian, M. Almasi-Kashi, Large scale ZnO nanorod-based UV sensor induced by optimal seed layer, Ceram Int. 42 (2016) 13421–13431.
[34] C.R. Michel, N.L. Lopez Contreras, M.A. Lopez-Alvarez, A.H. Martinez-Preciado, Gas selectivity of nanostructured $ZnSb_2O_6$ synthesized by a colloidal method, Sens. Actuators B 171 (2012) 686–690.
[35] J. Zhang, X. Liu, G. Neri, N. Pinna, Nanostructured materials for room-temperature gas sensors, Adv. Mater. 28 (2016) 795–831.
[36] A. Sharma, M. Tomar, V. Gupta, Low temperature operating SnO_2 thin film sensor loaded with WO_3 micro-discs with enhanced response for NO_2 gas, Sens. Actuators B 161 (2012) 1114–1118.
[37] Y. Cao, D. Jia, R. Wang, J. Luo, Rapid one-step room-temperature solid-state synthesis and formation mechanism of ZnO nanorods as H_2S-sensing materials, Solid State Electron. 82 (2013) 67–71.
[38] H.S. Woo, C.H. Kwak, I.D. Kim, J.H. Lee, Selective, sensitive, and reversible detection of H_2S using Mo-doped ZnO nanowire network sensors, J. Mater. Chem. A 2 (2014) 6412–6418.
[39] T. Yu, X. Cheng, X. Zhang, L. Sui, Y. Xu, S. Gao, H. Zhao, L. Huo, Highly sensitive H_2S detection sensors at low temperature based on hierarchically structured NiO porous nanowall arrays, J. Mater. Chem. A 3 (2015) 11991–11999.
[40] J. Hu, G. Yin, J. Chen, M. Ge, J. Lu, Z. Yang, D. He, An olive-shaped SnO_2 nanocrystal-based low concentration H_2S gas sensor with high sensitivity and selectivity, Phys. Chem. Chem. Phys. 17 (2015) 20537–20542.
[41] J. Tian, F. Pan, R. Xue, W. Zhang, X. Fang, Q. Liu, Y. Wang, Z. Zhang, D. Zhang, A highly sensitive room temperature H_2S gas sensor based on SnO_2 multi-tube arrays bio-templated from insect bristles, Dalton. 44 (2015) 7911–7916.
[42] J. Sukunta, A. Wisitsoraat, A. Tuantranont, S. Phanichphant, C. Liewhiran, Highly-sensitive H_2S sensors based on flame-made V-substituted SnO_2 sensing films, Sens. Actuators B 242 (2017) 1095–1107.
[43] Z. Song, Z. Wei, B. Wang, Z. Luo, S. Xu, W. Zhang, H. Yu, M. Li, Z. Huang, J. Zang, F. Yi, H. Liu, Sensitive room-temperature H2S gas sensors employing SnO_2 quantum wire/reduced graphene oxide nanocomposites, Chem. Mater. 28 (2016) 1205–1212.
[44] X. Li, Y. Wang, Y. Lei, Z. Gu, Highly sensitive H_2S sensor based on template-synthesized CuO nanowires, Rsc Advances 2 (2012) 2302–2307.
[45] W. Guo, L. Mei, J. Wen, J. Ma, High-response H_2S sensor based on ZnO/SnO_2 heterogeneous nanospheres, RSC Adv. 6 (2016) 15048–15053.
[46] X. Gao, Y. Sun, C. Zhu, C. Li, Q. Ouyang, Y. Chen, Highly sensitive and selective H_2S sensor based on porous $ZnFe_2O_4$ nanosheets, Sens. Actuators B 246 (2017) 662–672.
[47] L. Yin, D. Chen, M. Hu, H. Shi, D. Yang, B. Fan, G. Shao, R. Zhang, G. Shao, Microwave-assisted growth of In_2O_3 nanoparticles on WO_3 nanoplates to improve H_2S-sensing performance, J. Mater. Chem. A 2 (2014) 18867–18874.
[48] C. Zhao, B. Huang, E. Xie, J. Zhou, Z. Zhang, Improving gas-sensing properties of electrospun In_2O_3 nanotubes by Mg acceptor doping, Sens. Actuators B 207 (2015) 313–320.

[49] X. Liang, T.H. Kim, J.W. Yoon, C.H. Kwak, J.H. Lee, Ultrasensitive and ultraselective detection of H_2S using electrospun CuO-loaded In_2O_3 nanofiber sensors assisted by pulse heating, Sens. Actuators B 209 (2015) 934–942.
[50] J. Liu, W. Guo, F. Qu, C. Feng, C. Li, L. Zhu, J. Zhou, S. Ruan, W. Chen, V-doped In_2O_3 nanofibers for H_2S detection at low temperature, Ceram Int. 40 (2014) 6685–6689.
[51] W. Chen, Y. Liu, Z. Qin, Y. Wu, S. Li, P. Ai, A single Eu-doped In_2O_3 nanobelt device for selective H_2S detection, Sensors 15 (2015) 29950–29957.
[52] J. Kim, K. Yong, Mechanism study of ZnO nanorod-bundle sensors for H_2S gas sensing, J. Phys. Chem. C 115 (2011) 7218–7224.
[53] Z. Wen, L. Zhu, Y. Li, Z. Zhang, Z. Ye, Mesoporous Co_3O_4 nanoneedle arrays for high-performance gas sensor, Sensor Actuator B 203 (2014) 873–879.
[54] S.J. Chang, T.J. Hsueh, I.C. Chen, B.R. Huang, Highly sensitive ZnO nanowire CO sensors with the adsorption of Au nanoparticles, Nanotechnology 19 (2008).
[55] C. Balamurugan, D.W. Lee, A selective NH_3 gas sensor based on mesoporous p-type NiV_2O_6 semiconducting nanorods synthesized using solution method, Sens. Actuators B 192 (2014) 414–422.
[56] J. Yang, X. Wang, R. Xia, E. Muhire, M. Gao, Self-assembly in the synthesis of shelled ZnO hollow spheres and their UV sensors performance, Mater. Lett. 182 (2016) 10–14.
[57] L. Xu, B. Dong, Y. Wang, X. Bai, Q. Liu, H. Song, Electrospinning preparation and room temperature gas sensing properties of porous In_2O_3 nanotubes and nanowires, Sens. Actuators B 147 (2010) 531–538.